Vortical Flow Computations on Swept Flexible Wings Using Navier-Stokes Equations

Guru P. Guruswamy*
NASA Ames Research Center, Moffett Field, California 94035

A procedure to couple the Navier-Stokes solutions with modal structural equations of motion is presented for computing aeroelastic responses of swept flexible wings. The Navier-Stokes flow equations are solved by a finite-difference scheme with dynamic grids. The coupled aeroelastic equations of motion are solved using the linear-acceleration method. The configuration-adaptive dynamic grids are time-accurately generated using the aeroelasticlly deformed shape of the wing. The calculations are compared with the experiment when available. Effects of flexibility, sweep angle, and pitch rate are demonstrated for flows with vortices.

Nomenclature

A = pitch rate of ramp motion
a = speed of sound
C_p = coefficient of pressure
$\{d\}$ = displacement vector
E,F,G,Q = flux vectors in Cartesian coordinates
e = total energy per unit volume
$[L]$ = diagonal area matrix of the aerodynamic control points
$[M],[D],[K]$ = modal mass, damping, and stiffness matrices, respectively
P_r = Prandtl number
p = pressure
$\{q\}$ = generalized displacement vector
Re_c = Reynolds number based on the root chord
U = flight velocity
u,v,w = velocity components in x,y, and z directions, respectively
x,y,z = Cartesian coordinates
$\{Z\}$ = generalized force vector
α = angle of attack
γ = ratio of specific heats
Δ = difference between upper and lower surface pressure
κ = coefficient of thermal conductivity
λ = second coefficient of viscosity, $= -2/3\mu$
μ = coefficient of dynamic viscosity
ξ,η,ζ = generalized curvilinear coordinates
ρ = density
τ = nondimensional time
$[\phi]$ = modal displacement matrix

Subscripts and Superscripts

v = viscous quantities
∞ = freestream quantities
$\hat{(\ )}$ = quantities in generalized coordinate system
$\dot{(\ )}$ = first derivative with respect to time
$\ddot{(\ )}$ = second derivative with respect to time

Received April 17, 1989; revision received Sept. 6, 1989. Copyright ©1989 by the American Institute of Aeronautics and Astronautics, Inc. No copyright is asserted in the United States under Title 17, U.S. Code. The U.S. Government has a royalty-free license to exercise all rights under the copyright claimed herein for Governmental purposes. All other rights are reserved by the copyright owner.

*Research Scientist, Applied Computational Fluids Branch. Associate Fellow AIAA.

Introduction

FLOWS with vortices play an important role in the design and development of aircraft. In general, strong vortices form on a wing at large angles of attack. For wings with large sweep angles, strong vortices can form, even at moderate angles of attack. Formation of vortices changes the aerodynamic load distribution on a wing. Vortices formed on aircraft have been known to cause several types of instabilities such as wing rock for rigid delta wings[1] and aeroelastic oscillations for highly swept flexible wings.[2] Such instabilities can severely impair the performance of an aircraft. On the other hand, vortical flows can also play a positive role in the design of an aircraft. Vortical flows associated with rapid, unsteady motions can increase the unsteady lift, which can be used for maneuvering the aircraft.[3]

To date, most of the calculations for wings with vortical flows have been restricted to steady and unsteady computations on rigid wings. It is necessary to account for the wing flexibility in order to compute flows accurately. The aeroelastic deformation resulting from the flexibility of a wing can considerably change the nature of the flow. Strong interactions between the vortical flows and the structures can lead to sustained aeroelastic oscillations for highly swept wings.[4] Also, it is necessary to include the flexibility for proper correlations of computed data with experiments, particularly with those obtained from flight tests. In order to account for the flexibility of a wing, it is necessary to solve the aerodynamic and aeroelastic equations of motion simultaneously. In this work, the flow is modeled using the Navier-Stokes equations and is coupled with the aeroelastic equations of motion. The Navier-Stokes equations are required to model accurately the viscous effects on vortical flows.

The computer code developed for computing the unsteady aerodynamics and aeroelasticity of aircraft by using the Euler/Navier-Stokes equations is referred to as ENSAERO.[5] The capability of ENSAERO to compute aeroelastic responses by simultaneously integrating the Euler equations and the modal structural equations of motion, using aeroelastically adaptive dynamic grids, has been demonstrated.[5] The flow is solved by time-accurate, finite-difference schemes based on the Beam-Warming algorithm. Recently, the capability of ENSAERO was extended to couple solutions from the Navier-Stokes equations with the modal structural equations. The capability of ENSAERO to simulate vortical flows numerically on flexible rectangular wings is demonstrated in Ref. 6.

In this work, the capability of ENSAERO is extended to model the Euler/Navier-Stokes equations for swept wings. Computations are made for vortical-flow conditions about flexible swept wings, and the results are compared with available experiments. The formation of vortices and their dynamics on flexible wings is demonstrated, as are the effects of flexibility, sweep angle, and pitch rate for wings in unsteady ramp motion with vortical flows.

Aerodynamic Equations and Approximations

The strong, conservation-law form of the Navier-Stokes equations is used for shock-capturing purposes. The equations in Cartesian coordinates in nondimensional form can be written as[7]

$$\frac{\partial \boldsymbol{Q}}{\partial t}+\frac{\partial \boldsymbol{E}}{\partial x}+\frac{\partial \boldsymbol{F}}{\partial y}+\frac{\partial \boldsymbol{G}}{\partial z}=\frac{\partial \boldsymbol{E}_v}{\partial x}+\frac{\partial \boldsymbol{F}_v}{\partial y}+\frac{\partial \boldsymbol{G}_v}{\partial z} \tag{1}$$

where

$$\boldsymbol{Q}=\begin{bmatrix}\rho\\ \rho u\\ \rho v\\ \rho w\\ e\end{bmatrix}$$

$$\boldsymbol{E}=\begin{bmatrix}\rho u\\ \rho u^2+p\\ \rho uv\\ \rho uw\\ u(e+p)\end{bmatrix}\quad \boldsymbol{F}=\begin{bmatrix}\rho v\\ \rho uv\\ \rho v^2+p\\ \rho vw\\ v(e+p)\end{bmatrix}\quad \boldsymbol{G}=\begin{bmatrix}\rho w\\ \rho uw\\ \rho vw\\ \rho w^2+p\\ w(e+p)\end{bmatrix} \tag{2}$$

$$\boldsymbol{E}_v=Re_c^{-1}\begin{bmatrix}0\\ \tau_{xx}\\ \tau_{yx}\\ \tau_{zx}\\ \beta_x\end{bmatrix}\quad \boldsymbol{F}_v=Re_c^{-1}\begin{bmatrix}0\\ \tau_{xy}\\ \tau_{yy}\\ \tau_{zy}\\ \beta_y\end{bmatrix}\quad \boldsymbol{G}_v=Re_c^{-1}\begin{bmatrix}0\\ \tau_{xz}\\ \tau_{yz}\\ \tau_{zz}\\ \beta_z\end{bmatrix}$$

with

$$\begin{aligned}
\tau_{xx}&=\lambda(u_x+v_y+w_z)+2\mu u_x\\
\tau_{yy}&=\lambda(u_x+v_y+w_z)+2\mu v_y\\
\tau_{zz}&=\lambda(u_x+v_y+w_z)+2\mu w_z\\
\tau_{xy}&=\tau_{yx}=\mu(u_y+v_x)\\
\tau_{xz}&=\tau_{zx}=\mu(u_z+w_x)\\
\tau_{yz}&=\tau_{zy}=\mu(v_z+w_y)\\
\beta_x&=\gamma\kappa Pr^{-1}\partial_x e_I+u\tau_{xx}+v\tau_{xy}+w\tau_{xz}\\
\beta_y&=\gamma\kappa Pr^{-1}\partial_y e_I+u\tau_{yx}+v\tau_{yy}+w\tau_{yz}\\
\beta_z&=\gamma\kappa Pr^{-1}\partial_z e_I+u\tau_{zy}+v\tau_{zy}+w\tau_{zz}\\
e_I&=e\rho^{-1}-0.5(u^2+v^2+w^2)
\end{aligned} \tag{3}$$

The Cartesian velocity components u, v, and w are nondimensionalized by a_∞ (the freestream speed of sound); density ρ is nondimensionalized by ρ_∞; and the total energy per unit volume, e, is nondimensionalized by $\rho_\infty a_\infty^2$. Pressure can be found from the ideal-gas law as

$$p=(\gamma-1)\left[e-0.5\rho(u^2+v^2+w^2)\right] \tag{4}$$

To enhance numerical accuracy and efficiency and to handle boundary conditions more easily, the governing equations are transformed from Cartesian coordinates to general curvilinear coordinates, where

$$\begin{aligned}
\tau&=t\\
\xi&=\xi(x,y,z,t)\\
\eta&=\eta(x,y,z,t)\\
\zeta&=\zeta(x,y,z,t)
\end{aligned} \tag{5}$$

The resulting transformed equations are not much more complicated than the original Cartesian set and can be written in nondimensional form as

$$\frac{\partial}{\partial\tau}\hat{Q}+\frac{\partial}{\partial\xi}\left(\hat{E}-\hat{E}_v\right)+\frac{\partial}{\partial\eta}\left(\hat{F}-\hat{F}_v\right)+\frac{\partial}{\partial\zeta}\left(\hat{G}-\hat{G}_v\right)=0 \tag{6}$$

where $\hat{\ }$ indicates the transformed quantities.

In order to solve Eq. (6) for the full flowfield, a very fine grid is required throughout the flowfield. In high-Reynolds-number flows, the viscous effects are confirmed to a thin layer near rigid boundaries. Because of computer storage and speed limitations, in most practical cases, there are only enough grid points to resolve the gradients normal to the body by clustering the grid in the normal direction. Resolution along the body is similar to that used in inviscid flow. As a result, even though the full derivatives are retained in the equations, the gradients along the body are not resolved unless the streamwise and circumferential grid spacings are sufficiently small. Hence, for many Navier-Stokes computations, the viscous derivatives along the body are dropped. This leads to the thin-layer Navier-Stokes equations.[8] In this paper, the thin-layer Navier-Stokes form of Eq. (6) is used for modeling the flow.

The thin-layer model requires a boundary-layer type of coordinate system. In our case, the ξ and η directions are along the streamwise and spanwise directions of the wing, respectively, and viscous derivatives associated with these directions are dropped, whereas the terms in ζ, normal to the body, are retained and the body surface is mapped onto a constant ζ surface. Thus, Eq. (6) simplifies to

$$\partial_\tau\hat{Q}+\partial_\xi\hat{E}+\partial_\eta\hat{F}+\partial_\zeta\hat{G}=Re^{-1}\partial_\zeta\hat{S} \tag{7}$$

where

$$\hat{S}=J^{-1}\begin{bmatrix}
0\\
\mu(\zeta_x^2+\zeta_y^2+\zeta_z^2)u_\zeta+(\mu/3)(\zeta_x u_\zeta+\zeta_y v_\zeta+\zeta_z w_\zeta)\zeta_x\\
\mu(\zeta_x^2+\zeta_y^2+\zeta_z^2)v_\zeta+(\mu/3)(\zeta_x u_\zeta+\zeta_y v_\zeta+\zeta_z w_\zeta)\zeta_y\\
\mu(\zeta_x^2+\zeta_y^2+\zeta_z^2)w_\zeta+(\mu/3)(\zeta_x u_\zeta+\zeta_y v_\zeta+\zeta_z w_\zeta)\zeta_z\\
\left\{(\zeta_x^2+\zeta_y^2+\zeta_z^2)\left[0.5\mu(u^2+v^2+w^2)_\zeta\right.\right.\\
\quad\left.+\mu Pr^{-1}(\gamma-1)^{-1}(a^2)_\zeta\right]+(\mu/3)(\zeta_x u\\
\quad\left.+\zeta_y v+\zeta_z w)(\zeta_x u_\zeta+\zeta_y v_\zeta+\zeta_z w_\zeta)\right\}
\end{bmatrix} \tag{8}$$

It should be emphasized that the thin-layer approximation is valid only for high-Reynolds-number flows.

Several numerical schemes have been developed to solve Eq. (7). In this paper, the Pulliam-Chaussee diagonal form[8] of the implicit, approximate-factorization algorithm of Beam and Warming[9] is used.

The diagonal algorithm is fully implicit for the Euler equations. For the Navier-Stokes equations, the diagonal algorithm works as an explicit scheme since viscous terms in the right-hand side of Eq. (7) are treated explicitly. The diagonal algorithm is first-order accurate in time for both Euler and Navier-Stokes equations. Numerical exercises conducted during this work and previous work reported in Ref. 5 showed that the time-step size required to solve Eq. (7) is normally limited by accuracy rather than stability considerations. Therefore, the explicitness of the diagonal algorithm does not influence the computational efficiency in the solving of the Navier-Stokes equations.

Aeroelastic Equations of Motion

The governing aeroelastic equations of motion of a flexible wing are solved using the Rayleigh-Ritz method.[10] In this method, the resulting aeroelastic displacements at any time are expressed as a function of a finite set of assumed modes. The contribution of each assumed mode to the total motion is derived by Lagrange's equation. Furthermore, it is assumed that the deformation of the continuous wing structure can be represented by deflections at a set of discrete points. This assumption facilitates the use of discrete structural data, such as the modal vector, the modal stiffness matrix, and the modal mass matrix. These can be generated from a finite-element analysis or from experimental influence-coefficient measurements. In this study, the finite-element method is used to obtain the modal data.

It is assumed that the deformed shape of the wing can be represented by a set of discrete displacements at selected nodes. From the modal analysis, the displacement vector $\{d\}$ can be expressed as

$$\{d\} = [\phi]\{q\} \tag{9}$$

The final matrix form of the aeroelastic equations of motion is

$$[M]\{\ddot{q}\} + [D]\{\dot{q}\} + [K]\{q\} = \{Z\} \tag{10}$$

where $\{Z\}$, the aerodynamic force vector, is defined as $(\frac{1}{2})\rho U_\infty^2[\phi]^T[L]\{\Delta C_p\}$.

The aeroelastic matrix equation of motion, Eq. (10), is solved by a numerical integration technique based on the linear-acceleration method.[11]

Aeroelastic-Configuration-Adaptive Grids

One of the major problems in computational aerodynamics using the Euler/Navier-Stokes equations lies in the area of grid generation. For the case of steady flows, advanced techniques such as zonal grids[12] are being used. Grid-generation techniques for aeroelastic calculations that involve moving components are in an early stage of development. The effects of the aeroelastic-configuration-adaptive dynamic grids on the stability and accuracy of the numerical schemes are yet to be studied in detail.

This work developed an analytical grid-generation technique for aeroelastic applications. The scheme satisfies the general requirements of a grid required for implicit finite-difference schemes used in the analysis.[8] Some of the requirements are: 1) the grid lines intersect normal to the wing surface in the chordwise direction; 2) the grid cells are smoothly stretched away from the wing surface; 3) the outer boundaries are located far from the wing to minimize the effect of boundary reflections; and 4) the grids adapt to the deformed wing position at each time step. The type of grid used in this study is a C-H grid. The method by which the grid is generated at each time step, based on the aeroelastic position of the wing computed by using Eq. (10), is described.

At the end of each time step, the deformed shape of the wing is computed using Eq. (10). The ξ- and η-grid distributions on the grid surface corresponding to the wing surface (ζ grid index = 1) are obtained from previously assumed distributions. These distributions are selected to satisfy the general requirements of a grid for accurate computations. In this work, the grid in the ξ direction is selected so that the grid spacing is small near the wing and stretches exponentially to the outer boundaries. The grid near the leading edge is made finer than the rest of the wing in order to model the geometry accurately. In the spanwise direction, a uniformly distributed grid spacing is used on the wing. To model the wing tip, a finer grid space is used. Away from the wing tip, the η-grid spacing stretches exponentially. The ζ-grid spacing is computed at each time step using the deformed shape of the wing computed using Eq. (9). The ζ-grid lines start normal to the surface in the chordwise direction, and their spacing stretches exponentially to a fixed outer boundary. To prevent the outer boundaries from moving, the grid is sheared in the ζ direction. The metrics required in the computational domain are computed using the following relations:

$$\xi_t = -x_\tau\xi_x - y_\tau\xi_y - z_\tau\xi_z$$

$$\eta_t = -x_\tau\eta_x - y_\tau\eta_y - z_\tau\eta_z$$

$$\zeta_t = -x_\tau\zeta_x - y_\tau\zeta_y - z_\tau\zeta_z \tag{11}$$

The grid velocities x_τ, y_τ, and z_τ required in Eq. (11) are computed using the grids at new and old time levels. This adaptive grid-generation scheme is incorporated in ENSAERO. The ability of this scheme to compute accurate aeroelastic reponses has been demonstrated in Ref. 5.

The diagonal algorithm used in the present study computes time-accurate calculations in a geometrically nonconservative fashion. Geometric conservativeness can improve the accuracy of the results for moving grids. However, earlier studies have shown that the inclusion of geometric conservativeness has little effect on the solutions associated with the moving grids.[13] The time steps used for calculations with moving grids are typically small enough so that the error from geometric nonconservativeness is negligible for most practical purposes. The validation of computed results with experiments reported in Refs. 5 and 13 further supports the use of the diagonal scheme for computations associated with moving grids. In order to maintain the efficiency and robustness of the diagonal scheme, the present time-accurate computations are made without geometric conservativeness. Computational efficiency and robustness of the solution method are important for computationally intensive aeroelastic calculations with configuration-adaptive grids.

Results

Steady Pressure

The aerodynamic and aeroelastic solution procedures presented in the earlier sections are incorporated in ENSAERO. The current version of ENSAERO can compute flows over flexible wings using either the Euler or the Navier-Stokes equations. The same diagonal form of the Beam-Warming scheme is used to solve both equation sets. The resulting computer code is validated with experimental data for steady and unsteady flows over rectangular wings by using both the Euler and Navier-Stokes equations. Detailed results are presented in Refs. 5 and 6. In this paper, computations are made on swept rectangular wings.

In this work, all computations are made using a C-H type of grid. The grid dimensions are 91, 20, and 40 in streamwise, spanwise, and normal directions, respectively. This grid is fine enough to compute viscous flows using the thin-layer Navier-

Stokes equations. The grid spacing in the normal ζ direction off the surface of the wing is of the order 10^{-4} times the chord length. In all present computations, viscous terms are used only in the normal direction, which facilitates the use of the thin-layer Navier-Stokes equations. The grid spacing in the ξ direction on the surface is of the order 10^{-2} of the chord length. Fourteen span stations are used on the surface of the wing. The distribution of the grid in the spanwise direction is selected such that the spacing is uniform over most of the wing and becomes finer as it approaches the tip. The main objective of this work is to capture most of the flow details in the streamwise and normal directions. Though the present grid is adequate to model the spanwise three-dimensional effects, it is not designed to capture details of the flow near the tip. From numerical experiments, it is found that this grid spacing is adequate to model laminar flows, including shock waves and vortices on the wing.

Steady-state computations are made on a swept rectangular wing of aspect ratio 3.0 with NACA 0012 airfoil sections to validate the code. The leading-edge sweep angle is 20 deg. For this wing, steady experimental data are available in Ref. 14. Figure 1 shows the computed and measured steady pressures at $M_\infty = 0.695$, $\alpha = 2.0$ deg, and $Re_c = 5.95 \times 10^6$. The computed steady pressures compare well with the experimental data for all span stations. Slight discrepancies near the leading edge at the 25% semispan station can be attributed to the wind-tunnel wall effects. The current version of ENSAERO does not model the wind-tunnel walls.

In Fig. 2, the computed steady pressures at $M_\infty = 0.836$, $\alpha = 2.0$ deg, and $Re_c = 8.0 \times 10^6$ are shown. As reported in Ref. 15, the wind-tunnel wall effects are pronounced for this case. As a result, computations are not compared with the experiment; however, the results are compared with computations performed using the transonic Navier-Stokes (TNS) code.[15] In Fig. 2, the steady pressures from TNS are shown for the 50% semispan station. The comparison between the present results and those from TNS is favorable. Because both computations use the Beam-Warming scheme, the slight differences in the results can be attributed to the difference in the number of grid points. The number of grid points used in the present computations and in Ref. 15 are 72,800 and 165,321, respectively. Because of the coarseness of the present grid, the shock is slightly smeared.

The above-mentioned calculations show that the grid used in this work is adequate to model the transonic flows.

Unsteady Computations on Wings in Ramp Motions

Unsteady pressures are validated for a semi-infinite wing with NACA 0012 sections in a ramp-type pitching motion. This case is selected in order to validate the results from ENSAERO with unsteady measurements on two-dimensional wings (airfoils).[16] The results are computed by solving the Navier-Stokes equations in ENSAERO, which has the capability of modeling semi-infinite wings. Figure 3 shows the comparison between the computed and the experimental results obtained at $M_\infty = 0.30$, $Re_c = 2.5 \times 10^6$, and pitch rate $A = 0.02545$. The pitch rate A is defined as $\dot{\alpha}c/U_\infty$, where α is in radians. These computations are made using a time-step size of 1.0×10^{-3}. From numerical experiments, it was found that this time-step size is adequate to obtain a stable and accurate unsteady solution. The computed unsteady pressures shown in Fig. 3 compare well with the measured data.

Further unsteady and aeroelastic computations made using ENSAERO are validated with experiments for rectangular wings as reported in Refs. 5 and 6. In this section, the unsteady computations for rigid and flexible swept wings are made when the wings are undergoing ramp-type motion from 0 to 20 deg. Both wings are of an aspect ratio of 4.0, with

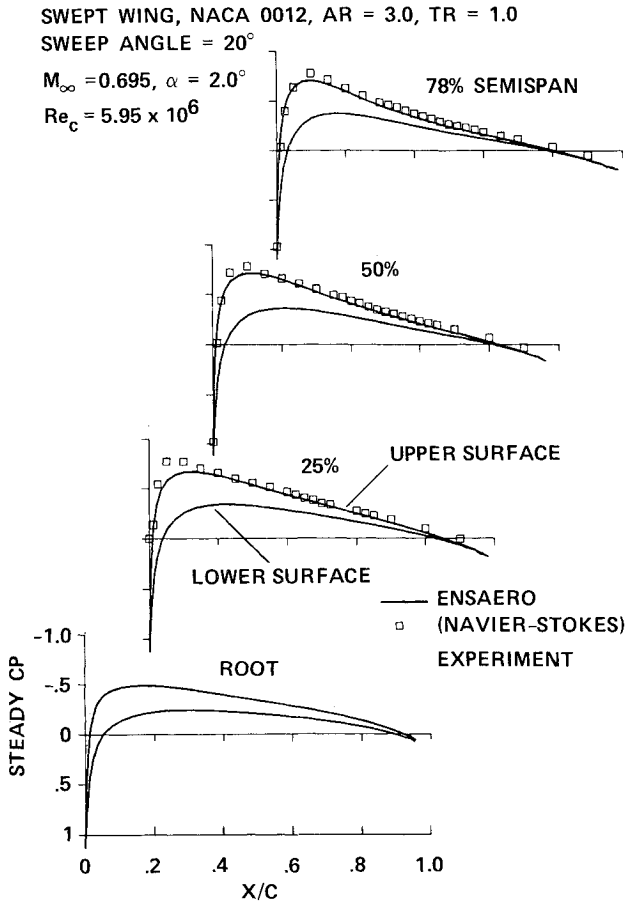

Fig. 1 Comparison between computed and measured steady pressures for 20-deg swept wing.

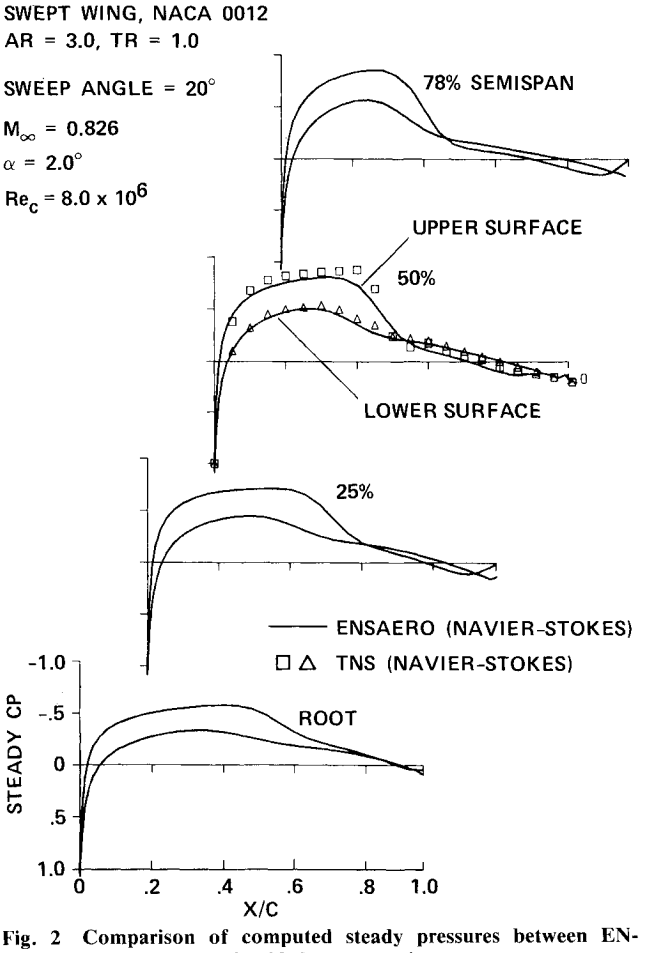

Fig. 2 Comparison of computed steady pressures between ENSAERO and TNS codes for 20-deg swept wing.

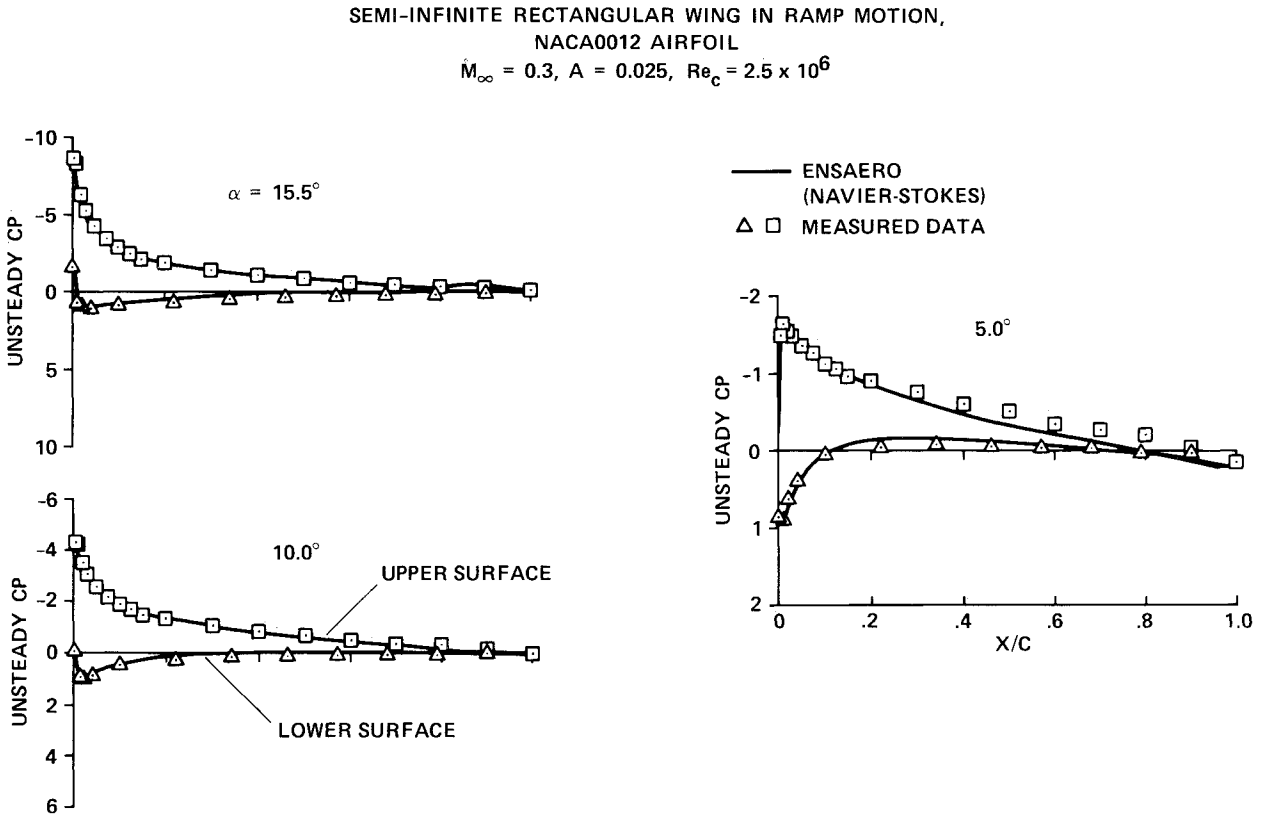

Fig. 3 Comparison between computed and measured unsteady pressures.

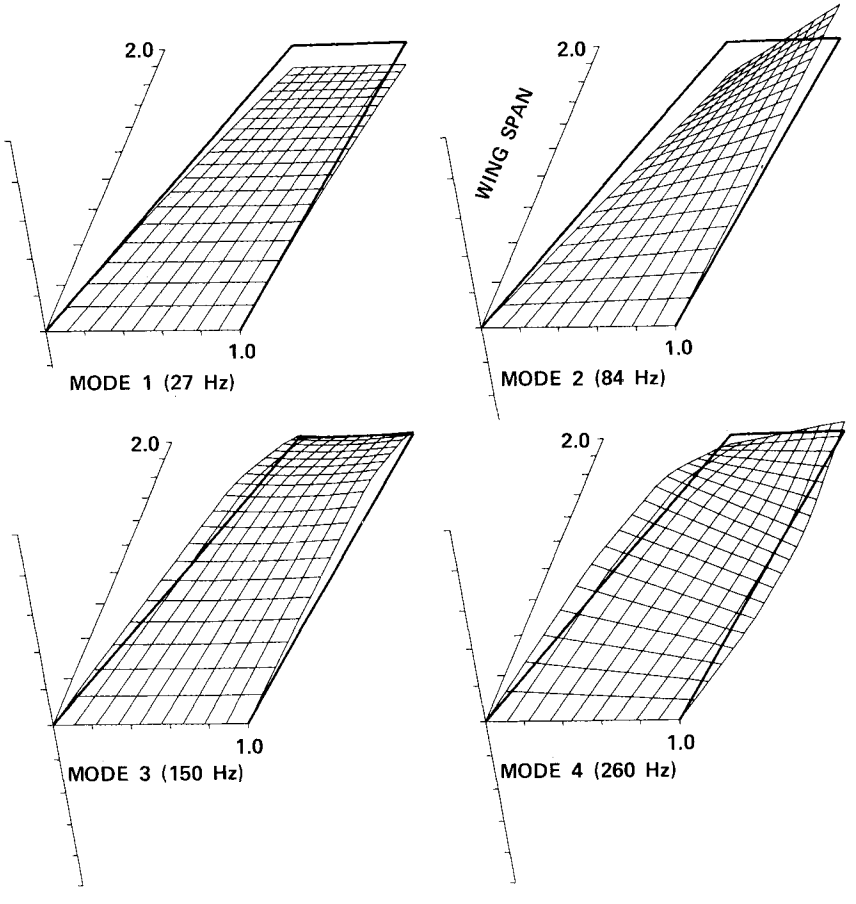

Fig. 4 Mode shapes of the swept rectangular wing.

NACA 0015 airfoil sections, and their leading-edge sweep angles are 30 deg. The structural properties of the flexible wing are modeled using four modes. The mode shapes and frequencies of the first four modes computed using the finite-element method are shown in Fig. 4. All computations, for both the rigid and flexible wings, are made at $M_\infty = 0.50$ and $Re_c = 2.0 \times 10^6$ by using a time-step size of 1.25×10^{-2}. From numerical experiments, it was found that the time-step size used is adequate to obtain a stable and accurate unsteady solution. Aeroelastic computations are made at a dynamic pressure of 2.0 psi.

Figure 5 shows unsteady pressures at four span stations for the rigid wing at $M_\infty = 0.50$, $Re_c = 2.0 \times 10^6$, and $A = 0.10$. The unsteady computations are started from the converged steady-state solution at $\alpha = 0$ deg. The results in Fig. 5 show the dynamics of vortex development. As the wing is pitched toward the maximum angle of attack, a rapid pressure decrease (increasing suction peak) occurs over the leading edge, which signals the formation of a leading-edge vortex. This vortex starts moving downstream rapidly after the wing has reached an angle of attack of about 18.0 deg. A similar phenomenon has been observed in an experimental study at a low Mach number.[17]

The same computations made on the rigid wing are also made on the flexible wing. Figure 6 shows results for the flexible wing, which has a pattern similar to the one shown in Fig. 5 for the rigid wing. However, the leading-edge vortex moves at a slightly faster rate than it does on the rigid wing. This is shown in Fig. 7 by plotting the unsteady pressures for both rigid and flexible wings at the nondimensional time of 7.0 The vortex core on the flexible wing is farther downstream than the vortex core on the rigid wing. Figure 8 shows the unsteady sectional-lift coefficients plotted against time for both the rigid wing and the flexible wing. At a given time, the lift over the flexible wing is higher than the lift over the rigid wing. This is due to the increase in the angle of attack caused by the wing flexibility. The deformed shape of the wing and the velocity contours in the freestream direction are shown in Fig. 9. The presence of the leading-edge vortex can also be seen in Fig. 9.

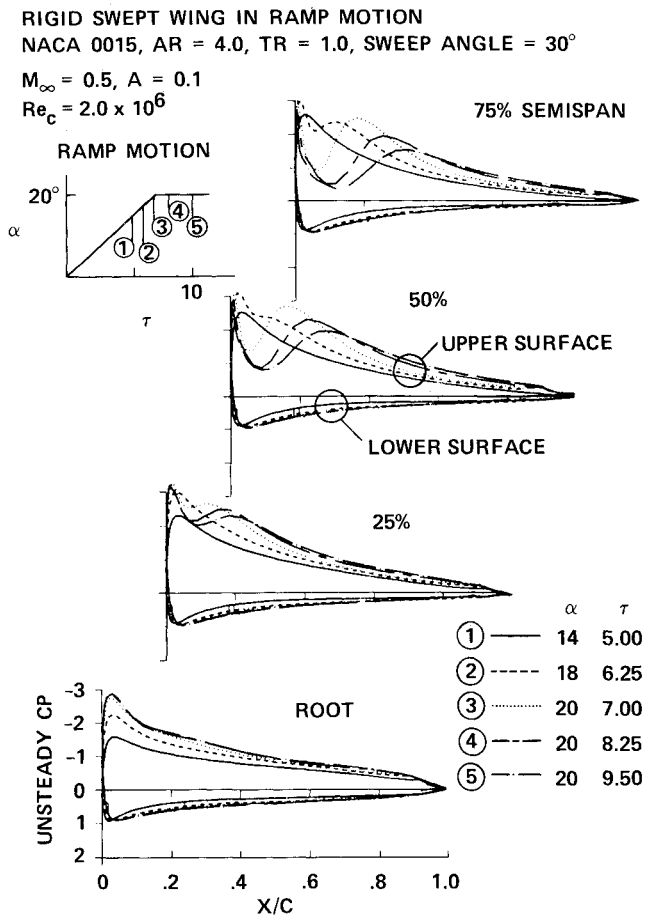

Fig. 5 Unsteady pressures on the swept rigid wing in ramp motion.

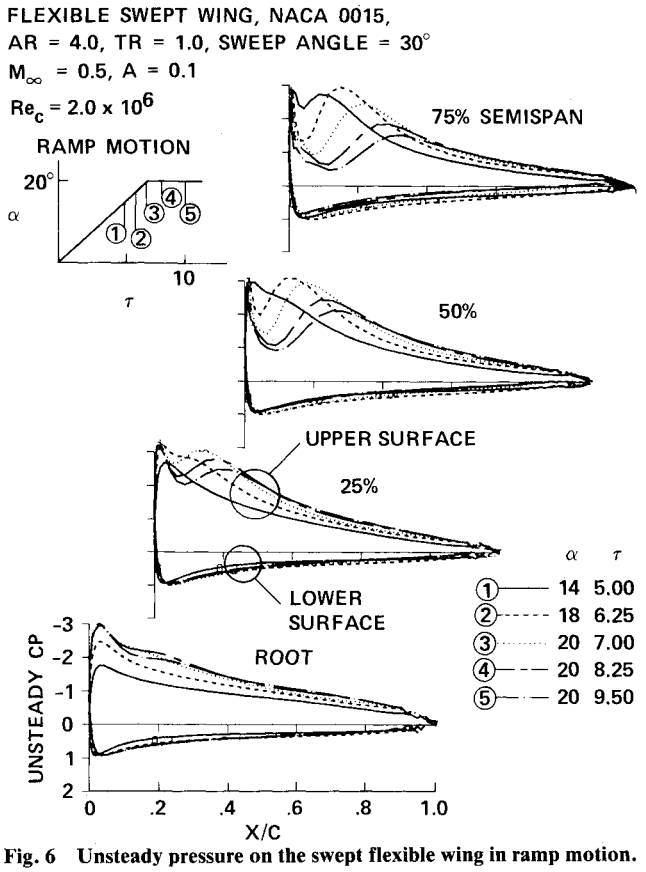

Fig. 6 Unsteady pressure on the swept flexible wing in ramp motion.

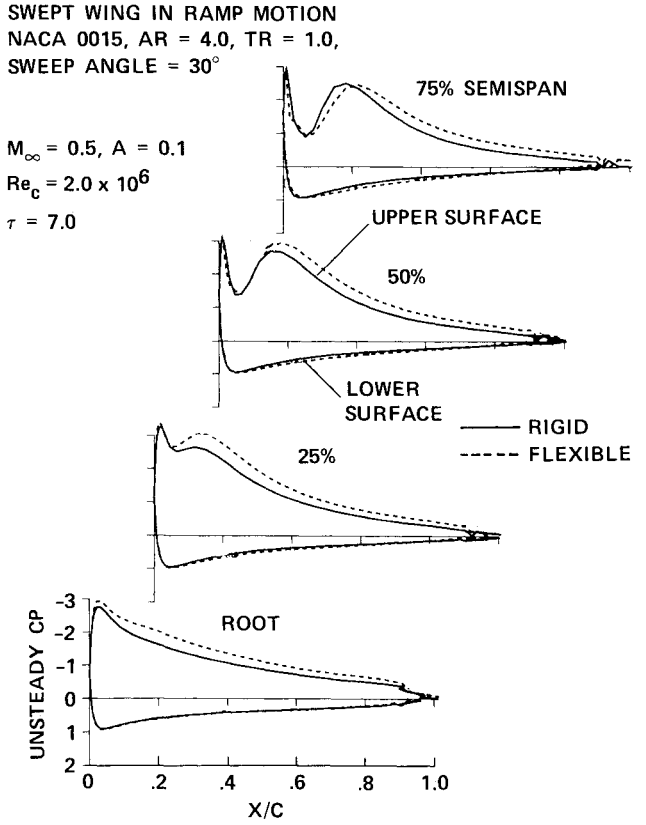

Fig. 7 Comparison of unsteady pressures between rigid and flexible swept wings.

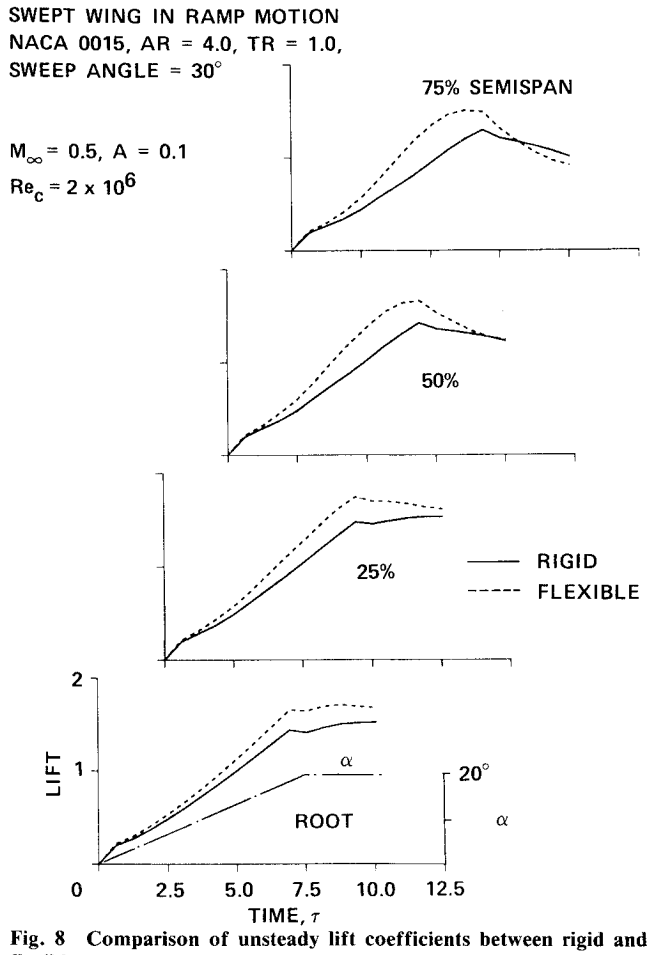

Fig. 8 Comparison of unsteady lift coefficients between rigid and flexible swept wings.

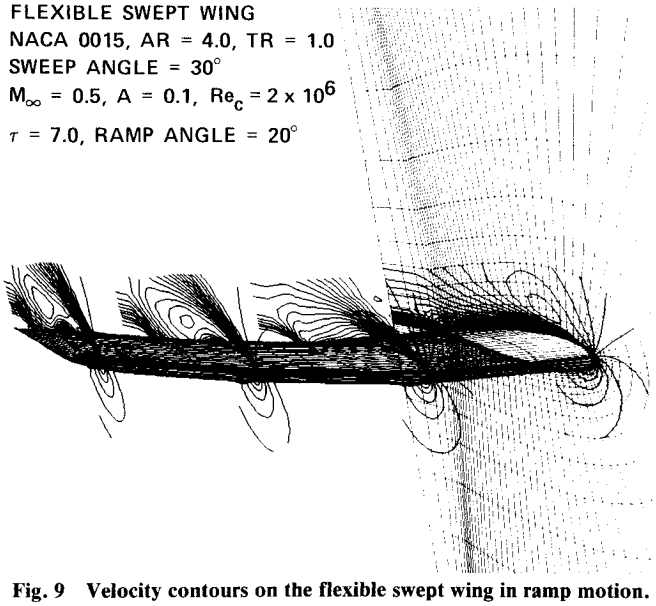

Fig. 9 Velocity contours on the flexible swept wing in ramp motion.

Computations are made for the unswept flexible wing at the same flow conditions as the swept flexible wing to study the effect of the sweep angle. The sweep effects on the unsteady pressures are illustrated in Fig. 10. The plots for the unswept wing do not differ much from section to section when compared to the plots for the swept wing. The unsteady pressures in Fig. 10, for $\tau = 7.0$, show that the vortex core for the unswept wing has convected downstream with almost the same speed for all four span sections; for the swept wing the vortex core has convected faster toward the tip.

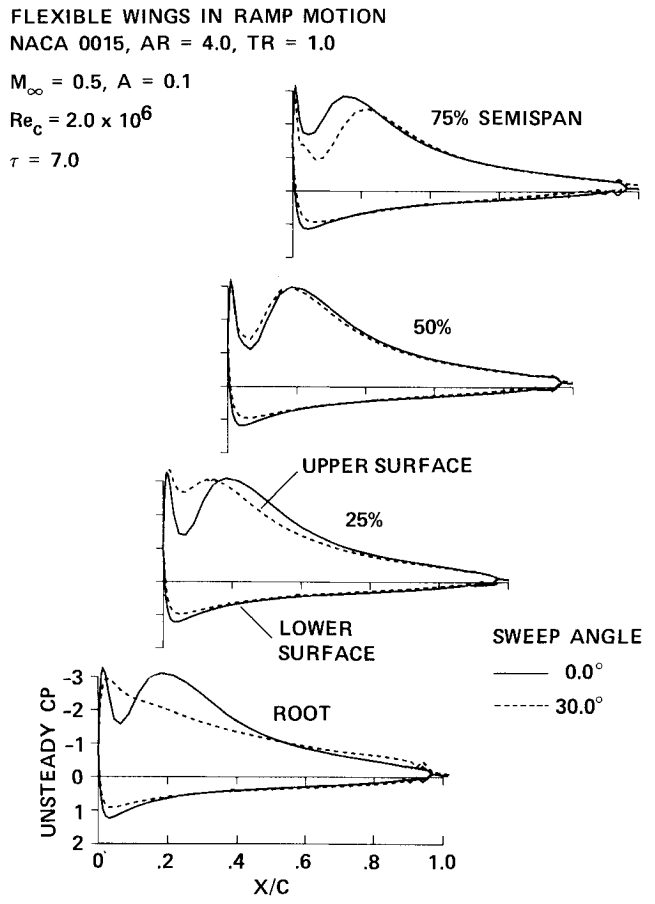

Fig. 10 Comparison of unsteady pressures between swept and unswept flexible wings.

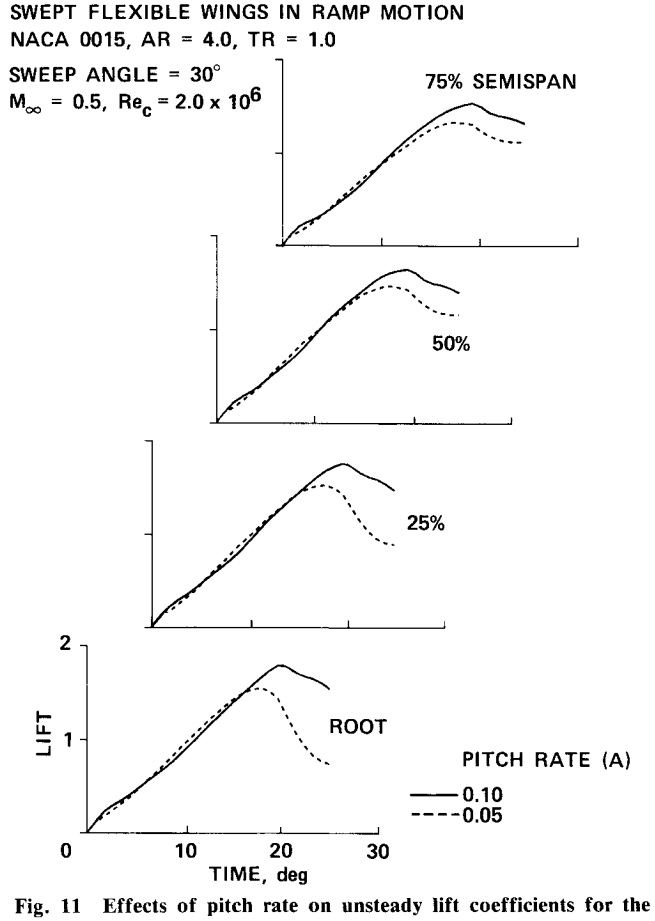

Fig. 11 Effects of pitch rate on unsteady lift coefficients for the swept wing.

One area where vortical flows play an important role is in increasing the dynamic lift. From earlier studies[3] on airfoils, it has been observed that the dynamic lift can be increased by increasing the pitch rates. Such increases in the dynamic lift can be used in maneuvering an aircraft.[3] Because the dynamic lift is an unsteady phenomenon and is associated with the presence of vortices, it is important to model it accurately. The present computational tool can be used to compute accurately the dynamic lift over wings, including the wing flexibility. To illustrate this further, computations are made for the swept flexible wing for a pitch rate $A = 0.05$, the results are compared with those obtained earlier for $A = 0.10$. The unsteady lifts are plotted against time in degrees in Fig. 11. The increase in the dynamic lift at the higher pitch rate, $A = 0.10$, can be seen in Fig. 11.

The foregoing computations were made on both CRAY-XMP48 and CRAY-2 computers available at Ames. The current version of ENSAERO runs at 60 MFLOPS (million floating point operations per second). The CPU time per time step per grid is 31×10^{-6} s, and the memory required per grid is 66 words.

Conclusions

The following conclusions can be made based on the present work.

1) A time-accurate numerical procedure has been developed for computing the unsteady flows on swept flexible wings using the Navier-Stokes equations with configuration-adaptive dynamic grids.

2) The computed results compare well with the available experimental data for steady and unsteady flows.

3) Coupling solutions from the Navier-Stokes equations with the modal structural equations of motion have been demonstrated for swept rectangular wings.

4) Unsteady computations for flows involving vortices are made on a flexible wing, and the effects of flexibility, sweep angle, and pitch rate on vortical flows have been demonstrated.

References

[1]Nguyen, L. E., Yip, L. P., and Chambers, J. R., "Self-Induced Wing Rock Oscillations of Slender Delta Wings," AIAA Paper 81-1883, Aug. 1981.

[2]Dobbs, S. K., and Miller, G. D., "Self-Induced Oscillation Wind Tunnel Test of a Variable Sweep Wing," AIAA Paper 85-0739, April 1985.

[3]Mabey, D. G., "On the Prospects for Increasing Dynamic Lift," *Aeronautical Journal of the Royal Aeronautical Society*, March 1988, pp. 95-105.

[4]Guruswamy, G. P., Goorjian, P. M., Ide, H., and Miller, G. D., "Transonic Aeroelastic Analysis of the B-1 Wing," *Journal of Aircraft*, Vol. 23, July 1986, pp. 547-553.

[5]Guruswamy, G. P., "Unsteady Aerodynamic and Aeroelastic Calculations of Wings Using Euler Equations," *AIAA Journal*, Vol. 28, March 1990, pp. 461-469.

[6]Guruswamy, G. P., "Numerical Simulation of Vortical Flows on Flexible Wings," AIAA Paper 89-0537, Jan. 1989.

[7]Peyret, R., and Viviand, H., "Computation of Viscous Compressible Flows Based on Navier-Stokes Equations," AGARD AG-212, 1975.

[8]Pulliam, T. H., and Chaussee, D. S., "A Diagonal Form of an Implicit Approximate Factorization Algorithm," *Journal of Computational Physics*, Vol. 39, Feb. 1981, pp. 347-363.

[9]Beam, R., and Warming, R. F., "An Implicit Finite-Difference Algorithm for Hyperbolic Systems in Conservation Law Form," *Journal of Computational Physics*, Vol. 22, Sept. 1976, pp. 87-110.

[10]Bisplinghoff, R. L., Ashley, H., and Halfman, R. L., *Aeroelasticity*, Addison Wesley, Reading, MA, 1957.

[11]Guruswamy, G. P., and Yang, T. Y., "Aeroelastic Time Response Analysis of Thin Airfoils by Transonic Code LTRAN2," *Computers and Fluids*, Vol. 9, Dec. 1980, pp. 409-425.

[12]Flores, J., Chaderjian, N., and Sorenson, R., "The Numerical Simulation of Transonic Separated Flow About the Complete F-16A," AIAA Paper 88-2506, June 1988.

[13]Huff, D. L., "Numerical Simulations of Unsteady, Viscous, Transonic Flow Over Isolated and Cascaded Airfoils Using a Deforming Grid," AIAA Paper 87-1316, June 1987.

[14]Lockman, W. K., and Seegmiller, H. L., "An Experimental Investigation of the Subcritical and Supercritical Flow About a Swept Semispan Wing," NASA TM-84367, 1983.

[15]Kaynak, U., Holst, T. L., and Cantwell, B. J., "Computations of Transonic Separated Wing Flows Using an Euler/Navier-Stokes Zonal Approach," NASA TM-88311, 1986.

[16] Landon, R. H., "NACA0012. Oscillatory and Transient Pitching," Compendium of Unsteady Aerodynamic Measurements, AGARD-R-702, Aug. 1982.

[17]Robinson, M. C., and Wissler, J. B., "Unsteady Surface Pressure Measurements on a Pitching Rectangular Wing," AIAA Paper 88-0328, Jan. 1988.